Experimental and theoretical analysis of transient grating generation and detection of acoustic waveguide modes in ultrathin solids

Jeffrey S. Meth, C. D. Marshall, and M. D. Fayer
Department of Chemistry, Stanford University, Stanford, California 94305

(Received 22 September 1989; accepted for publication 22 November 1989)

A full theoretical analysis of and experimental evidence for the optical generation and detection of acoustic waveguide modes (Lamb waves) in ultrathin solids using the transient grating (TG) technique is presented. The driving force due to the TG excitation is derived for a free, isotropic plate. In contrast to a bulk isotropic material in which a single wave is excited, the TG excites a number of modes with a variety of frequencies but with the same tangential component of the wavevector. The frequencies beat, resulting in a complex time-dependent signal. Experimental results are presented for anthracene sublimation flakes. In addition to discussing the general features of Lamb wave generation, we also discuss the effects of mounting the crystal on a substrate, of varying the fringe spacing, of resonant probing, and of polarized detection. The nature of Lamb waves in anisotropic materials is illustrated, and the extent to which the isotropic theory can be applied to anisotropic systems is discussed.

I. INTRODUCTION

In this paper we present a theoretical treatment of the optical generation and detection of acoustic waveguide modes in ultrathin solids. Aside from its importance as basic science, understanding this problem can provide a method for investigating the material properties of ultrathin solids. Phonon spectra of solids provide information about thermodynamic properties such as the heat capacity, while acoustic velocity and attenuation measurements yield mechanical properties such as the compliance.[1-3] This information can be used to study intermolecular interactions. The scattering and attenuation of acoustic phonons can be used to investigate strains and defects in a solid.[4] Recently there has been considerable interest in ultrathin ($< 1\,\mu$m) materials in electronics,[5] coatings,[6] optics,[7] and other areas. To investigate ultrathin materials it is necessary to generate and detect a variety of ultrasonic frequencies and wavevectors in a situation which is not readily amenable to conventional acoustic wave methods[4] which involve contacting transducers to the sample. Here we report an optical holographic method (transient grating)[8] for the generation and detection of acoustic waveguide modes (Lamb waves[9]) in ultrathin materials. The transient grating (TG) method does not require mechanical contact with the sample, and therefore can be applied to delicate materials.

The coherent generation and detection of phonons in bulk condensed matter systems using the TG technique has been previously described in detail.[8] In the TG experiment (Fig. 1), two picosecond laser pulses are overlapped spatially and temporally in a sample. The interference between the two pulses of wavelength λ creates a fringe pattern in the sample where the fringe spacing d is related to the angle between the beams, θ, by the relation

$$d = \lambda/2 \sin(\theta/2) = 2\pi/\beta. \quad (1)$$

The electromagnetic energy in the interference pattern couples to the sample, creating acoustic waves.[8] In a bulk material, the wavelength of the acoustic waves is determined by the fringe spacing. In a waveguide with the grating pointed in the z direction, the z component of the wavevector of the waveguide-mode, which will be referred to as the propagation constant, is determined by the grating. The acoustic waves (density waves) produce a time-dependent modulation of the sample's density, and hence generate a time-dependent oscillation in the real and imaginary part of the index of refraction of the medium. The time-dependent oscillation of the index of refraction spatially mimics the optical interference pattern and acts as a Bragg diffraction grating. A third, variably time delayed, picosecond pulse diffracts from the induced acoustic wave grating. The diffracted signal beam intensity is related to the magnitudes and the time dependencies of the optically induced density waves.

TG acoustic wave experiments on waveguides are fundamentally different from the analogous experiments conducted on thick samples. Until recently, this technique has only been applied to bulk samples. In this paper, we present experiments performed on acoustic waveguides and a theoretical treatment of the phenomenon. In a waveguide it is necessary to take into account the effects of the surfaces.[9] For a thin plate surrounded by vacuum (x and z define the plane of the plate and y is the perpendicular to the plane), the acoustic waves are reflected by the surfaces. At a surface, the longitudinal waves (compressional, k-vector parallel to the polarization vector) couple with the shear waves polarized in the yz plane. A compressional wave incident on the surface reflects into a compressional and a shear wave, and a shear wave incident on a surface reflects into a shear and a compressional wave. Thus the normal modes in the waveguide are combinations of shear and longitudinal waves.[9] The shear and longitudinal components of the Lamb wave are referred to as partial waves. For a normal mode, the motion of a microscopic volume element is elliptical. The axes of the ellipse are parallel and perpendicular to the plate surfaces, and the eccentricity of the ellipse varies with the waveguide normal mode. These normal modes are known as Lamb waves,[9] and can be separated into two families, symmetric and antisymmetric, depending on the symmetry of

 0021-8979/90/073362-16$03.00

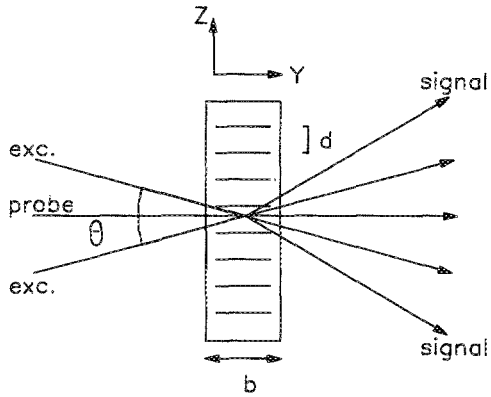

FIG. 1. The transient grating beam configuration. θ is the crossing angle of the beams, b is the thickness of the sample, and d is the fringe spacing.

the velocity fields when reflected in the xz plane (Fig. 2).

The existence of these two families of modes can be understood by considering the dimensionality of the waveguide. A bulk system is treated as infinite in all dimensions, enabling the phonon dispersion relationships for each dimension to be decoupled. In a planar waveguide with the y-dimension finite, the dispersion relations for propagation in the yz plane are coupled. Thus, for each value of the propagation constant, there is an entire family of modes labeled by different values of the shear and longitudinal y components of the wavevector.

There are two mechanisms[10] by which the TG technique generates a driving force to launch acoustic waves: heating and stimulated Brillouin scattering (SBS). If the frequency of the exciting laser radiation is chosen to excite a vibrationally excited state, fast radiationless relaxation will deposit heat into the sample with a spatial period mimicking the period of the grating's fringe spacing. This heat causes thermal expansion, launching counterpropagating acoustic waves with a propagation constant equal to the grating's wavevector.[11]. The heat creates a thermal strain in the sample that dissipates with the thermal diffusivity of the material. This is on the order of microseconds for typical grating fringe spacings and appears constant on the time scale of the grating experiment, which is nanoseconds. The strain due to

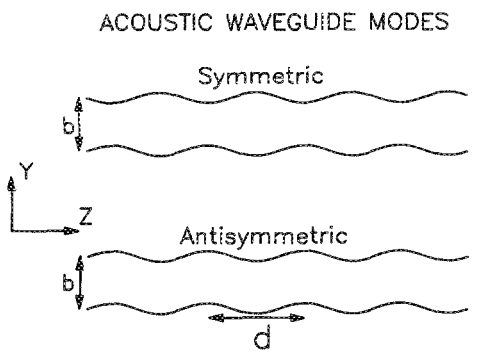

FIG. 2. Symmetric (dilatational) and antisymmetric (flexural) acoustic waveguide modes. d is the fringe spacing, b is the thickness. The modes are symmetric and antisymmetric with respect to reflection in the xz plane, the plane of the waveguide. x is out of the plane of the figure.

the acoustic waves beats against that of the thermal strain to produce a time dependence which, for a single wave in a bulk sample, is proportional to $1 - \cos(\omega t)$. SBS involves the direct coupling of the electromagnetic field to the strain field via the photoelastic tensor, and the time dependence of the induced strain is proportional to $\sin(\omega t)$. There is no heat deposited in the sample via SBS. The differences between the driving forces for the two mechanisms will be discussed in the theoretical section.

For the experiments performed here, the heating mechanism is responsible for generating the observed acoustic waves. In our experiments, we excite with a frequency close to the origin of the first singlet exciton band in anthracene. Absorption (generation of excited states) in a pure molecular crystal can only occur in conjunction with phonon scattering.[12] It is experimentally observed that almost all of the light that is not reflected is absorbed by the system. If the typical phonon energy involved in scattering releases 1 cm^{-1}, and if 10^{12} photons are absorbed (the number of photons in a 0.5 μJ pulse), it is still possible to create a temperature rise of ~ 0.01 K locally in the crystal. In anthracene, the magnitude of the force due to this temperature change will overwhelm the force induced by SBS, even when the known resonant enhancement of the photoelastic tensor at an optical transition is taken into account.[13,14] For this reason, we present complete theoretical results for the heating mechanism only, although we will discuss the theory of SBS generation to a limited extent in the theoretical section.

In a bulk crystal, there can be only three frequencies (one quasilongitudinal and two quasishear in the most general case) generated by the TG experiment. By aligning the grating along a crystal symmetry axis of the material, it is possible to generate a single acoustic wave in a bulk material. Even when the grating is aligned along a crystal symmetry axis of the waveguide, more than one mode must be excited for the physical continuity of stresses and strains to be realized. The precise combination of modes that will be generated will depend on the specific excitation conditions such as the damping of the electromagnetic field, and the fringe spacing and the thickness. Furthermore, the phase velocity of the Lamb modes which are generated will not possess the same phase velocity as measured in the bulk material.

The TG initial conditions generate a coherent superposition of Lamb waves which possess the same value for the propagation constant in the material. The generation of a coherent superposition of modes in k space is a unique property of the TG experiment. This is fundamentally different from a transducer, which drives a system at a certain frequency. The information gained by studying the response of a system in a transient grating experiment can complement or replace that gained by frequency-driven experiments to provide a more complete physical understanding of the system in question.

From the theory, several basic features of the TG excitation of waveguides can be discerned. First, if one uses a driving force which is not damped (very weak absorption), then only symmetric modes can be excited. This is because the driving field is symmetric with respect to the mirror plane xz. Conversely, if the driving force is damped (optical ab-

sorption) both symmetric and antisymmetric modes are excited. Second, the use of perpendicularly polarized pulses will generate vertically polarized (x-polarized) shear waves in analogy to the generation of shear waves in bulk materials.[15] Shear wave generation in waveguides has not yet been demonstrated.

In the material presented below, we describe the theory of the generation of Lamb modes in a free, isotropic plate for the initial conditions created by the transient grating technique. We also present transient grating experiments performed on ultrathin anthracene sublimation flakes. There are three main features that will be explored in the experimental section. First, we will demonstrate how the grating can distinguish between a Lamb wave whose motion makes it primarily a surface wave from one whose motion occurs mainly in the interior of the sample. Second, we will demonstrate the effects of observing the diffracted signal through a polarizer. It is known that for a bulk sample longitudinal stresses will not rotate the polarization of the light that is diffracted by it, while shear stresses will rotate the polarization of diffracted light.[15] We will discuss the extension of this phenomenon into the waveguide regime and show how this technique allows one to separate quasilongitudinal modes from quasishear modes. Third, we will demonstrate how to construct the dispersion relations for a material by performing the transient grating at a variety of fringe spacings. This is very important, as it allows a convenient method for determining the dispersion relationships of anisotropic materials.

Another point that will be addressed is the influence on diffraction of the spatial dependence of the Lamb waves in the y dimension. The amplitude of diffraction from a particular Lamb wave is not simply proportional to the amplitude of the wave that is generated in the initial superposition created by the TG experiment.

The experiments were performed with the grating directed along the crystallographic b axis. In the monoclinic space group $P2_1/a$ (C_{2h}^5 in Schoenflies' notation), which includes anthracene, the b axis is a twofold screw axis. This simplifies the anisotropic nature of the normal modes that are generated by the transient grating, as will be discussed in detail later.

Throughout the analysis, we will demonstrate the feasibility of applying the isotropic model for a free plate to anthracene, an anisotropic system. Since the isotropic model is the only theory which can be expressed analytically, it is important to access the extent to which it can be used to describe anisotropic systems.

The theory that is presented here is developed for a free flake in a vacuum. In the experiments both free flakes and mounted flakes are examined. The flake, when free mounted, is still in an inert gaseous atmosphere. Since the frequencies generated are ultrasonic, no acoustic energy leaks from the sample, and the vacuum approximation is still valid. We have also performed experiments on flakes which were optically contacted to a fused silica substrate. This changes the boundary conditions, but does not change the essence of the problem. The theory for acoustic wave propagation in a waveguide invokes stress-free boundary conditions: the y components of the stress tensor, T_{yy}, T_{yz}, T_{yx}, must be zero at the boundaries of the flake. For a free flake in a vacuum, the vacuum cannot support any strain and the analysis proceeds from there. If the flake is in contact with a substrate, however, the substrate will have some strain at its boundary with the flake to meet the boundary condition. Unlike a free, isotropic flake, where the Rayleigh–Lamb frequency equations used for calculating the dispersion can be expressed analytically,[9] these equations cannot be expressed analytically for a flake mounted on a substrate. Although the eigenvalues and eigenvectors of a mounted flake will be slightly different from those of a free flake, the essential physics of the problem remains unchanged. A superposition of normal modes of the system is generated and these modes propagate in the sample.

This situation is analogous to that for optical waveguides. In a planar optical waveguide surrounded on either side by media with different indices of refraction, an electromagnetic wave can be totally internally reflected from one surface, but it can partially transmit energy through the other surface. In an acoustic waveguide, a wave which is totally internally reflected from one surface may leak some of its energy through the other surface and into the third medium. These are known as leaky waves. Experimentally, if a leaky wave is generated, it will damp noticeably on the timescale of the experiment. However, the known values for the velocity of sound in fused silica[16] ensures that the generated acoustic waves will remain trapped inside the anthracene waveguide, because the difference in acoustic velocities provides a large acoustic impedance mismatch at the surface.

II. EXPERIMENTAL PROCEDURES

The output of a Q switched, mode-locked Nd:YAG laser operating at a 600 Hz repetition rate is beamsplit and each beam is doubled and used to synchronously pump two cavity dumped dye lasers. One 1.06 μm pulse is selected via a Pockels cell, and it is summed with the cavity-dumped pulse from one of the dye lasers to provide a tunable source of near-UV, 30 ps, 3 μJ pulses. The tunability ranges from 365–410 nm. The other dye laser is cavity dumped to provide a tunable probe wavelength in the range of 560–860 nm with similar pulse duration and energy. The near-UV color is used for exciting the sample. To probe the sample, either a piece of the UV pulse or a pulse from the visible dye laser was used.

Because the samples are very thin, the Bragg diffraction condition is relaxed, and it is not necessary to bring the probe beam into the sample at the Bragg angle. Instead, the probe is brought in normal to the sample, and it bisects the angle made by the excitation beams. This simplifies changing the fringe spacing.

The signal is detected with a photomultiplier and a lock-in amplifier. A retroreflector mounted on a motorized delay line scans the delay between the probe pulse and the excitation pulses. A computer digitizes the signal intensity and a voltage which is proportional to the probe pulse delay, then averages several scans of the delay line to improve the signal-to-noise ratio.

The time domain data obtained in this manner displays many frequencies which beat against one another. To ana-

lyze the data and determine these frequencies, a fast-Fourier transform (FFT) routine was applied to the time domain data to provide frequency domain spectra of the scans. This enables us to directly observe the individual components of the acoustic superposition state that is generated by the transient grating excitation.

Anthracene (Kodak X480) was extensively zone refined ($\sim$400 passes). Since this anthracene is synthetic, it is not necessary to chromatograph it to remove carbazole, a naturally occurring impurity. Only the middle of the zone-refining tube was used for growing sublimation flakes. The sublimation flakes were grown under $\sim$75 Torr of Ar and the heat bath was maintained at 130 °C.

The effect of pressure on the morphology of the sublimation flakes is straightforward. If the pressure is too low, $\sim$25 Torr, the anthracene sublimes as a powder and there is no flake formation. As the pressure increases, the flakes form with very large surface area (up to 1 cm^2) and they are very thin ($\sim 1\ \mu m$). A further increase in pressure increases the thickness of the flakes and decreases their surface area. Flakes of 10 μm can be produced with a surface area of about 4 mm^2 with a pressure of 400 Torr. Increasing the temperature to 140 °C does not noticeably change the dynamics of flake growth. However, a noticeable decrease in the rate of flake growth is observed when the temperature is lowered to 125 °C. To produce harvestable flakes, the charge of anthracene must be fine ground before introducing it into the sublimator. A charge of $\sim$50 mg is sufficient for producing many flakes.

To produce mounted samples, the harvested flakes are placed on fused silica discs. Because of static charges, the flakes become optically contacted to the substrate. Observation of the flakes under crossed polarizers reveals that there are vast regions of the flakes which are strain free. Another glass flat is epoxied onto the first one under an Ar atmosphere to protect the flake from oxidation. Prepared in this way, a flake will not damage for up to three weeks of daily use, provided the laser power is kept sufficiently low.

For the experiments performed on free flakes, the samples were mounted in small paper envelopes similar to those diagramed by Philpott.[17] These were slipped into 1-mm path length cuvettes and sealed under an Ar atmosphere.

There are several techniques for measuring the thickness of the flake. One of these is to measure the absorption spectra of the flake using a transmission geometry. Interference fringes can be observed in the red edge of the absorption. Using literature values for the index of refraction in this wavelength regime,[18] one can calculate the thickness. This thickness is then correlated with the optical density (OD) at the absorption minimum between the (0,0) and (0,1) transitions, which occurs at about 380 nm. We have found that to $\pm$ 10%, a 1 μm flake has, for a-polarized light, an OD = 1.0 at this minimum at room temperature. This provides a useful calibration for determining the thickness of subsequent samples. This technique is nondestructive and can be performed before other data are taken. Another technique for measuring the thickness involves measuring the surface area of the flake, dissolving it in a known amount of solvent, then recording the absorption spectrum. By knowing the absorption coefficient, one can determine the concentration, hence the weight, of the sample. Then, by knowing the density of anthracene, one can calculate the thickness. This technique is destructive and can only be performed after the other experiments are completed.

III. THEORY

The optical excitation of Lamb waves via the TG experiment is essentially the problem of a driven wave equation. To solve this problem, one must first know the spatial nature of the Lamb waves that will be excited. This involves calculating the dispersion relations for the normal modes of the planar waveguide using numbers appropriate for anthracene. Next one must determine the force that drives the wave equation. We consider an undamped electromagnetic field as well as an electromagnetic field which is damped as it traverses the sample (to account for absorption). Fourier techniques are then used to decompose the driving force, which can be treated as an instantaneous impulse, into a coherent superposition of Lamb waves. This decomposition determines the Lamb waves which are excited in the sample. By knowing the amplitude and frequency of these waves, it is possible to calculate the time dependent intensity of the signal pulse which is diffracted from the acoustic wave phase grating. This calculation must be performed numerically because of the y dependence of the strain of the Lamb waves. The results of this calculation show that the contribution of a particular mode to the diffracted observable is not directly proportional to its amplitude and is greatly influenced by the spatial shape of the mode.

A. Acoustic equations

The acoustic field equations are given, in contracted notation, as follows:

$$\mathbf{S} = \nabla \cdot \mathbf{u} \quad \text{or} \quad \frac{\partial \mathbf{S}}{\partial t} = \nabla \cdot \mathbf{v}. \tag{2}$$

This is the strain-displacement relationship;

$$\nabla \cdot \mathbf{T} = \rho_0 \frac{\partial^2 \mathbf{u}}{\partial t^2} - \mathbf{F}_{\text{body}} = \rho_0 \frac{\partial \mathbf{v}}{\partial t} - \mathbf{F}_{\text{body}} \tag{3}$$

is the equation of motion, and

$$\mathbf{T} = c \cdot \mathbf{S} \quad \text{or} \quad \mathbf{S} = s \cdot \mathbf{T}, \tag{4}$$

where $c = s^{-1}$ is the Hooke's law constitutive relation.

In these equations, u (cm) and v (cm/s) are 3×1 column vectors representing the displacement and velocity, respectively. In contracted notation, S (unitless) and T (dyne/cm^2) are 6×1 column vectors representing strain and stress, respectively, and c (dyne/cm^2) and s (cm^2/dyne) are 6×6 fourth-rank tensors representing elastic compliances and stiffnesses. F_{body} (dyne/cm^3) is the 3×1 column vector representing the applied body force on the system. ∇ (1/cm) is the 6×3 spatial differentiation matrix.[11]

Since the TG experiment possesses mirror symmetry with respect to the z axis, which is aligned along the b axis of the crystal, one expects to generate counterpropagating Lamb waves. The Lamb waves will have a velocity field dis-

tribution which is

$$v = v_y\hat{y} + v_z\hat{z}, \tag{5}$$

where

$$v_{y,s} = \omega/\beta^2[\,-k_{tl}\sin(k_{tl}y)\cos(k_{ts}b/2) - (\beta^2 - k_{ts}^2)/2k_{ts}\cos(k_{tl}b/2) \times \sin(k_{ts}y)\,]\cos(\beta z), \tag{6a}$$

$$v_{z,s} = -\omega/\beta\,[\cos(k_{tl}y)\cos(k_{ts}b/2) - (\beta^2 - k_{ts}^2)/2\beta^2\cos(k_{tl}b/2) \times \cos(k_{ts}y)\,]\sin(\beta z), \tag{6b}$$

for the symmetric modes, and

$$v_{y,a} = \omega/\beta^2[\,k_{tl}\cos(k_{tl}y)\sin(k_{ts}b/2) + (\beta^2 - k_{ts}^2)/2k_{ts}\sin(k_{tl}b/2) \times \cos(k_{ts}y)\,]\cos(\beta z), \tag{7a}$$

$$v_{z,a} = -\omega/\beta\,[\sin(k_{tl}y)\sin(k_{ts}b/2) - (\beta^2 - k_{ts}^2)/2\beta^2\sin(k_{tl}b/2) \times \sin(k_{ts}y)\,]\sin(\beta z), \tag{7b}$$

for the antisymmetric modes. In the above equations, k_{tl} and k_{ts} are the transverse components of the longitudinal and shear partial waves and are related to β and ω by the formulas:

$$\beta^2 + k_{tl}^2 = \omega^2/V_l^2, \tag{8a}$$

$$\beta^2 + k_{ts}^2 = \omega^2/V_s^2, \tag{8b}$$

where V_l and V_s are the longitudinal and shear velocities, respectively, of the bulk material.[9]

By inserting the expressions for the velocity fields into the acoustic field Eq.(3), one can calculate the internal stress due to a specific Lamb wave. These expressions have the form:

$$F_{\rm int} = F_{{\rm int},y}\hat{y} + F_{{\rm int},z}\hat{z}, \tag{9}$$

where

$$F_{y,s} = \rho\omega^2/\beta^2[\,k_{tl}\sin(k_{tl}y)\cos(k_{ts}b/2) + (\beta^2 - k_{ts}^2)/2k_{ts}\cos(k_{tl}b/2) \times \sin(k_{ts}y)\,]\cos(\beta z), \tag{10a}$$

$$F_{z,s} = \rho\omega^2/\beta\,[\cos(k_{tl}y)\cos(k_{ts}b/2) - (\beta^2 - k_{ts}^2)/2\beta^2\cos(k_{tl}b/2) \times \cos(k_{ts}y)\,]\sin\beta z, \tag{10b}$$

for the symmetric modes, and

$$F_{y,a} = -\rho\omega^2/\beta^2[\,k_{tl}\cos(k_{tl}y)\sin(k_{ts}b/2) + (\beta^2 - k_{ts}^2)/2k_{ts}\sin(k_{tl}b/2) \times \cos(k_{ts}y)\,]\cos(\beta z), \tag{11a}$$

$$F_{z,a} = \rho\omega^2/\beta\,[\sin(k_{tl}y)\sin(k_{ts}b/2) - (\beta^2 - k_{ts}^2)/2\beta^2\sin(k_{tl}b/2) \times \sin(k_{ts}y)\,]\sin\beta z, \tag{11b}$$

for the antisymmetric modes.

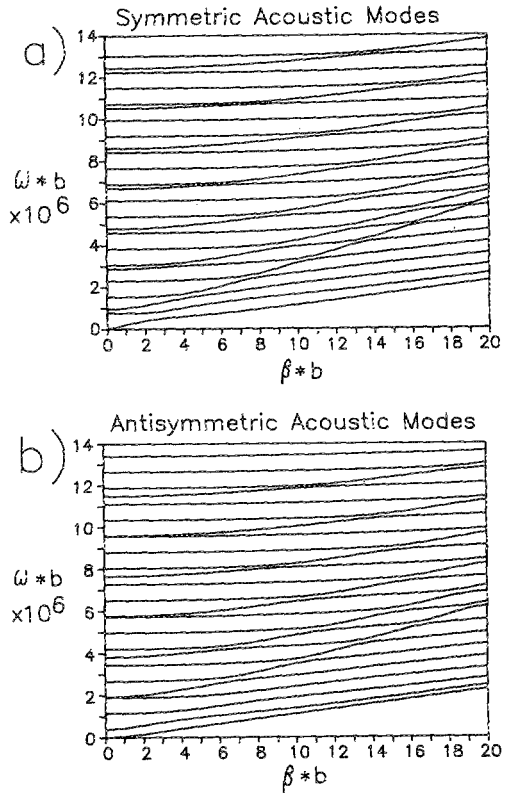

FIG. 3. Dispersion relations for a free, isotropic plate waveguide. (a) Symmetric Lamb modes. (b) Antisymmetric Lamb modes. The calculations were performed using constants for an anthracene crystal modeled as isotropic.

The wavevector dependence of the Lamb mode frequencies was calculated using the Rayleigh–Lamb frequency equations for a free, isotropic plate.[9] These equations were solved numerically for k_{tl}, k_{ts}, and ω and the results are displayed graphically in Fig. 3(a) for the symmetric modes and in Fig. 3(b) for the antisymmetric modes. The calculations employed constants appropriate for an anthracene single crystal, but treated it as isotropic. Since the data to be presented were taken with the grating wavevector directed along the crystallographic b axis, the values of the velocities of sound for the y-polarized shear wave and the longitudinal wave in the b direction were used for V_s and V_l, respectively. These values, and those for the elastic constants, were taken from the work of Afanaseva.[19] In their work, $V_s = 1.22\times10^5$ cm/s and $V_l = 3.05\times10^5$ cm/s. The plane of the plate corresponds to the anthracene ab plane. While it is possible to do the calculations for the actual anisotropic solid, the complexity of the calculation is vastly magnified because the Rayleigh–Lamb equations mentioned above cannot be expressed analytically. Notice that in Fig. 3 the axes are scaled by b, the thickness of the waveguide. Scaled in this manner, the dispersion relations have the same shape for any sample thickness.

Usually, normal modes are orthogonal to one another. For Lamb waves, the orthogonality condition can be expressed as:

$$F_{s\beta}F_{r\beta'} = \delta_{sr}\times\delta_{\beta\beta'}, \tag{12}$$

where the s, r refers to the symmetry of the mode and β, β'

refers to the propagation constant of the mode. From this expression, one sees that the symmetric modes (s) are orthogonal to the antisymmetric modes (r) and that modes with different values of the propagation constant are orthogonal. However, Lamb waves of the same propagation constant but different frequencies are not orthogonal to one another. This is a peculiar circumstance and occurs due to the stress-free boundary conditions used in deriving the Lamb modes, and can be easily proven using Green's theorem.[20] It can also be shown that the Lamb waves are linearly independent and that they span the Hilbert space representing displacements in the waveguide. This property is the result of the fact that the Lamb waves are the normal modes of a two-dimensional system. Just as phonons in one dimension can represent any deformation in that dimension, Lamb waves can represent any deformation in two dimensions. These properties insure that there is a unique decomposition of the driving force into a superposition of Lamb modes.

The internal forces in Eqs. (9)–(11) are normalized so that the calculated amplitudes are unitless and all the expressions for forces, velocities, strains, etc., have the proper units. We set

$$\left(\frac{\rho\omega^2}{\beta^2}\right)^2 = \int_0^d \int_{-b/2}^{b/2} (N_{\text{int},j})^2 F_{\text{int},j} F_{\text{int},j}\, dy\, dz, \qquad (13)$$

where $N_{\text{int},j}$ is the normalization constant for that mode. Note that $y = 0$ represents the middle of the waveguide.

B. Transient grating driving force

To derive the driving force induced by the TG, consider a waveguide where the grating wavevector is directed along the z zaxis and the y direction is normal to the plate. Absorption followed by radiationless relaxation releases an amount of heat q (cal/mol) into the lattice leading to a spatially varying temperature increase given by

$$\Delta T(y,z) = \Delta T_{\max}/2(1+\cos\beta z) \times \exp[-\alpha y]\exp[-\alpha b/2], \qquad (14)$$

where $\beta = 2\pi/d$ is the wavevector of the grating, α is the absorption coefficient. $\Delta T_{\max} = q\,(1-\exp[-\alpha b])/\rho_0 C_v$, where ρ_0 is the unperturbed density, b is the thickness of the waveguide, and C_v is the constant volume heat capacity.[11] The exponential term in the expression for $\Delta T_{\max}$ is needed to conserve energy. If there is no absorption by the sample, then there is no temperature change.

The strain caused by thermal expansion is related to ΔT by the relation

$$\mathbf{S} = \gamma \cdot \Delta T \qquad (15)$$

where γ is the 3×3 tensor representing the linear coefficient of thermal expansion. Since this is an isotropic treatment, γ is the same in all directions.

The applied body force is represented as F_{body}:

$$F_{\text{body}} = -\nabla\cdot T = -\nabla\cdot(c\cdot S), \qquad (16)$$

$$F_{\text{body}} = F_y\,\hat{y} + F_z\hat{z},$$

$$F_y = -A\exp[-\alpha y]\cos(\beta z)(c_{12}+c_{44}/2)\alpha\beta, \qquad (17a)$$

$$F_z = A\exp[-\alpha y]\sin(\beta z)(c_{44}/2\alpha^2 - c_{11}\beta^2), \qquad (17b)$$

where $A = (c_{11}+2c_{12})\gamma\exp[-\alpha b/2]\Delta T_{\max}/c_{11}\beta$.

One can understand the origin of this driving force in the following manner.[11,21] The heating of the sample takes place impulsively, meaning that the laser pulse duration is short compared to the period of any generated Lamb wave. Radiationless relaxation is fast, so the temperature gradient exists immediately after optical excitation. The driving force acts as an acceleration impulse, imparting finite material velocities at time $t = 0$. Although there are finite velocities at $t = 0$, the material has not had time to move, so there are no displacements. This implies that the total strain and the total stress must be zero. The system has not yet had a chance to undergo thermal expansion because thermal expansion occurs on a timescale equivalent to the time needed for an acoustic wave to travel half of a fringe spacing.

Thermal expansion and the launching of acoustic waves occur concurrently. The process of thermal expansion is completed in approximately half of the acoustic period. When thermal expansion is complete, the acoustic waves that are launched are at maximum density excursion and the density proceeds to oscillate from there in a cosinusoidal fashion. Since this occurs at a time that is halfway through an acoustic period, the time dependence of the acoustic wave appears to be $\cos(\omega t)$.

In approximately the first half-period, the system goes from having no strain to having a thermal strain and an acoustic strain. Because the system is an ultrathin waveguide, thermal expansion causes the surface of the waveguide to corrugate, with the waveguide becoming thicker in the peaks of the interference pattern where the temperature has been increased. The waves that are launched produce strain which then beats against the thermal strain of the corrugated waveguide. Since the corrugation is not large the Lamb modes remain the normal modes for the waveguide. The exact details of the launching of the acoustic waves will influence only the very short time behavior of the system, but are not important on the time scale of interest,[21] i.e., the time scale is long compared to an acoustic period.

It is important to notice the $\cos\beta z$ term in Eq. (17a) and the $\sin\beta z$ term in Eq. (17b). These terms demonstrate that the transient grating driving force is one which drives the system at a certain wavevector. This is in contrast to a transducer, which drives the system at a certain frequency. When a waveguide is driven at a given frequency, all modes with that frequency are excited, even though their wavevectors are of different magnitudes. Similarly, when a waveguide is driven at a certain propagation constant, all modes with that propagation constant will be excited. These modes will have various k_{ts} and k_{tl} and thus varying frequencies. The superposition of modes created by the TG can be identified by drawing a vertical line in Fig. 3 at the proper value of $\beta\times b$ and marking where the line intersects the dispersion relations for the individual modes. The amplitudes of excitation of the modes are calculated below. The value of ω/β gives the phase velocity of the wave that will be seen in the diffracted-signal. The TG creates a coherent superposition of waveguide modes which all possess the same propagation constant. A transducer can only drive a system at a single frequency, but the transient grating, due to the impulsive nature of the driving force, can drive a system at a constant

wavevector and many frequencies. This is the fundamental difference between mechanical and optical excitation of a waveguide.

For the case of SBS, one can show that the spatial dependence of the driving field has the form:

$$F_{\mathrm{SBS}} = F_y\hat{y} + F_z\hat{z},$$

$$F_y = -1/8\pi\, p_{12}\alpha E^2 \exp[-t^2\Gamma^2/2] \times \exp[-\alpha y]\exp[-\alpha b/2]\cos\beta z, \quad (18a)$$

$$F_z = -1/8\pi\, p_{12}\beta E^2 \exp[-t^2\Gamma^2/2] \times \exp[-\alpha y]\exp[-\alpha b/2]\sin\beta z. \quad (18b)$$

This is presented for a polarized excitation beams with the grating along the b axis, where p_{12} is the appropriate element of the photoelastic tensor and E^2 is the square of the electric field.

Comparison of the magnitudes of the driving forces in Eqs. (17) and (18) essentially involves comparing $c_{22}\gamma\Delta T_{\max}$ with $p_{12}E^2/8\pi$. With $\Delta T_{\max} \sim 0.01$ K, $\gamma \sim 10^{-4}$ K^{-1},[22] and $c_{22} \sim 10^{11}$ dyne/cm^2,[23] the first term has a magnitude of $\sim 10^5$ dyne/cm^2. For the second term, consider that 1 μJ in 30 ps implies an intensity of 3×10^4 W, distributed over an area of $\sim 10^{-3}$ cm^2 (300-μm sport sizes), lead to a value of $E^2 \sim 10^4$ dyne/cm^2. Since at room temperature the resonantly enhanced value of p is 4 at the maximum,[13] the second term has a magnitude of $\sim 2\times 10^3$ dyne/cm^2. Thus, it is reasonable to conclude that heating is the predominant mechanism of acoustic wave generation in these experiments.

SBS will become important for systems in which absorptive heating is essentially zero.[10] Presently, SBS can be performed on samples only when the excitation frequency is off-resonance and the incident energy is very high. Even under these circumstances, two photon or overtone absorptive heating can dominate.[10]. Experiments have been limited by the magnitude of the photoelastic coefficients, which are typically on the order of 1. However, in samples which do not absorb, SBS can provide an avenue for acoustic wave generation (see Ref. 10).

Now that the normal nodes are enumerated and the driving force has been determined, one can express the applied body force as a superposition of internal forces:

$$\sum a_m N_{\mathrm{int},s,m} F_{\mathrm{int},s,m}(y,z) + \sum b_m N_{\mathrm{int},a,n} F_{\mathrm{int},a,n}(y,z) = F_{\mathrm{body}}(y,z), \quad (19)$$

where the a_m and b_n are the unitless amplitude coefficients of the Lamb waves that are generated.

To solve for the amplitudes a_m, b_n, one multiplies Eq. (19) by a normal mode then integrates. Since the modes excited by the transient grating are not orthogonal, one obtains a matrix representing the overlap between the different modes:

$$\Phi_{jk} = \int_0^d \int_{-b/2}^{b/2} N_{\mathrm{int},s,j} N_{\mathrm{int},s,k} F_{\mathrm{int},s,j} F_{\mathrm{int},s,k}\, dy\, dz, \quad (20a)$$

for the symmetric modes, and

$$\Psi_{jk} = \int_0^d \int_{-b/2}^{b/2} N_{\mathrm{int},a,j} N_{\mathrm{int},a,k} F_{\mathrm{int},a,j} F_{\mathrm{int},a,k}\, dy\, dz, \quad (20b)$$

for the antisymmetric modes.

By representing the driving force as a sum of symmetric and antisymmetric forces, and using the fact that the symmetric Lamb modes are orthogonal to the antisymmetric modes, one arrives at the following two matrix equations which need to be inverted:

$$\Phi \cdot A = G_{\mathrm{body},s}, \quad (21a)$$

$$\Psi \cdot B = G_{\mathrm{body},a}, \quad (21b)$$

where G is a column vector representing the overlap between the applied body force and the Lamb waves. The individual elements of G are

$$G_{\mathrm{body},sj} = \int_0^d \int_{-b/2}^{b/2} N_{\mathrm{int},s,j} F_{\mathrm{int},s,j} F_{\mathrm{body}}(y,z)\, dy\, dz, \quad (22a)$$

for the symmetric modes, and:

$$G_{\mathrm{body},aj} = \int_0^d \int_{-b/2}^{b/2} N_{\mathrm{int},a,j} F_{\mathrm{int},a,j} F_{\mathrm{body}}(y,z)\, dy\, dz, \quad (22b)$$

for the antisymmetric modes.

Here, A and B are column vectors whose elements are the a_m and the b_n of Eq. (19) and represent the amplitudes of the Lamb waves. These equations are inverted numerically to yield the unitless amplitudes of the generated Lamb waves. The input parameters in the model, aside from the material properties such as elastic constants and density, are just the fringe spacing, the attenuation of the excitation beams by absorption, and the thickness of the waveguide.

C. Detection by diffraction from the superposition of Lamb waves

The diffraction of light by ultrasonic waves has been discussed in the literature.[10,15,24] and will be presented here for a monoclinic crystal. Simplification to the isotropic case is straightforward. Physically, the acoustic strain produces a spatially varying density in the waveguide, which modifies the index of refraction in a spatially periodic manner. The coupling between the strain field and the dielectric tensor is phenomenologically described by the fourth-rank photoelastic tensor, which has the same symmetry properties as the elastic tensor. It is not the dielectric tensor itself which is affected by the strain, rather it is the change in the impermeability (inverse dielectric) tensor which is related to the strain by:

$$\delta\nu_i = p_{ij} S_j \quad (23)$$

where p is the fourth rank photoelastic tensor and $\delta\nu_i$ is the change in the ith element of the inverse dielectric tensor. The impermeability tensor possesses the same symmetry as the dielectric tensor. The strain that appears in Eq. (23) is the total acoustic strain. It is the sum of two terms, the time independent strain caused by thermal expansion, and the time dependent strain which is the superposition of the Lamb waves calculated above.

For a monoclinic crystal with y being the twofold axis, the dielectric tensor has the form:

$$\epsilon = n^2 = \begin{bmatrix} \epsilon_1 & 0 & \epsilon_5 \\ 0 & \epsilon_2 & 0 \\ \epsilon_5 & 0 & \epsilon_3 \end{bmatrix} \quad (24)$$

and its inverse has the form:

$$\epsilon^{-1} = \nu = \begin{bmatrix} \nu_1 & 0 & \nu_5 \\ 0 & \nu_2 & 0 \\ \nu_5 & 0 & \nu_3 \end{bmatrix}$$

$$= [\epsilon_2(\epsilon_1\epsilon_3 - \epsilon_5^2)]^{-1} \begin{bmatrix} \epsilon_2\epsilon_3 & 0 & -\epsilon_2\epsilon_5 \\ 0 & \epsilon_1\epsilon_3 - \epsilon_5^2 & 0 \\ -\epsilon_2\epsilon_5 & 0 & \epsilon_2\epsilon_1 \end{bmatrix}. \quad (25)$$

When the perturbation is added, the impermeability tensor becomes:

$$\nu + \delta\nu = \begin{bmatrix} \nu_1 + \delta\nu_1 & \delta\nu_6 & \nu_5 + \delta\nu_5 \\ \delta\nu_6 & \nu_2 + \delta\nu_2 & \delta\nu_4 \\ \nu_5 + \delta\nu_5 & \delta\nu_4 & \nu_3 + \delta\nu_3 \end{bmatrix}. \quad (26)$$

This tensor is reinverted to give the modified dielectric tensor. Since the magnitude of the perturbation $\delta\nu$ is $\mathcal{O}(10^{-5})$, terms $\mathcal{O}(\delta\nu^2)$ will be dropped upon inversion. This yields a modified dielectric tensor of the form:

$$\epsilon' = \{(\nu_2 + \delta\nu_2)[(\nu_1 + \delta\nu_1)(\nu_3 + \delta\nu_3) - (\nu_5 + \delta\nu_5)^2]\}^{-1}$$
$$\begin{bmatrix} (\nu_2 + \delta\nu_2)(\nu_3 + \delta\nu_3) & \nu_5\delta\nu_4 - \nu_3\delta\nu_6 & -(\nu_2 + \delta\nu_2)(\nu_5 + \delta\nu_5) \\ \nu_5\delta\nu_4 - \nu_3\delta\nu_6 & (\nu_1 + \delta\nu_1)(\nu_3 + \delta\nu_3) - (\nu_5 + \delta\nu_5)^2 & \nu_5\delta\nu_6 - \nu_1\delta\nu_4 \\ -(\nu_2 + \delta\nu_2)(\nu_5 + \delta\nu_5) & \nu_5\delta\nu_6 - \nu_1\delta\nu_4 & (\nu_2 + \delta\nu_2)(\nu_1 + \delta\nu_1) \end{bmatrix}. \quad (27)$$

From the form of this tensor, one can associate the polarization of the diffracted probe pulse with the nature of the strain in the sample. Longitudinal strains in the sample, S_{xx}, S_{yy}, S_{zz}, do not rotate the polarization of the E-field of the probe because they only appear in the diagonal terms of ϵ'. Shear strains S_{yz}, S_{xz}, S_{xy}, rotate the polarization of the E-field of the probe by 90° because they only appear in the off-diagonal terms of ϵ'. This enables more information to be obtained from the system by placing a polarizer in front of the photodetector that measures the signal intensity. Frequencies that correspond to modes that have substantial shear nature will be present in data taken when the analyzing polarizer is perpendicular to the polarization of the incoming E field. Similarly, modes that are predominantly longitudinal in character will be observed when the analyzing polarization is parallel to that of the probing E field.

The diffraction efficiency for a grating in the low diffraction limit is given by:

$$\eta(\omega) = \exp[-2.3\, D_{\rm av}(\omega)/\cos\varphi\,](\pi b/\lambda_p \cos\varphi)^2 \times\{[\Delta k(\omega)]^2 + [\Delta n(\omega)]^2\}, \quad (28)$$

where $D_{\rm av}(\omega)$ is the average optical density at λ_p, the probe wavelength with frequency ω, and $\Delta k(\omega)$ and $\Delta n(\omega)$ are the peak-null differences in the imaginary and real parts of the index of refraction.[10]

For the purposes of this work, $\Delta k(\omega)$ can be expressed as the sum of four contributions:

$$\Delta k(\omega) = \Delta k_{\rm ex} + \Delta k_p + \Delta k_T + \Delta k_s, \quad (29)$$

where $\Delta k_{\rm ex}$ is the change induced by excited states in the sample; Δk_p is the change in the index as a function of density due to the presence of acoustic waves; Δk_T represents the change in the imaginary part of the refractive index caused by a change in temperature[25]; and Δk_s is the spectral shift term[10] again produced by the transient grating induced density changes. All of the components of $\Delta k(\omega)$ will only be observed when the probe beam is resonant with an optical transition. For application to a pure molecular crystal such as anthracene, the order of magnitude arguments used to eliminate Δk_p and Δk_s from consideration in a low-concentration mixed crystal[10] are not applicable here, and there is no reason to believe that these terms will not be observed.

Similarly, the $\Delta n(\omega)$ can be expressed as the sum of four contributions:

$$\Delta n(\omega) = \Delta n_{\rm ex} + \Delta n_p + \Delta n_T + \Delta n_s, \quad (30)$$

where $\Delta n_{\rm ex}$, Δn_p, Δn_T, and Δn_s are the real analogs of the imaginary effects described above. When a nonresonant probe is used to monitor the grating, only the Δn_p and Δn_T terms will contribute to diffraction. When a resonant probe is used, the $\Delta n_{\rm ex}$ term will dominate the expression. Since the diffraction is proportional to the square of $\Delta n(\omega)$, the Δn_p, Δn_T, and Δn_s terms will be enhanced by their crossproducts with $\Delta n_{\rm ex}$.

There is a complication involving the diffraction of light from a varying index of refraction that has not been addressed in the literature, and this pertains to the y dependence of the variation in the index of refraction. The equations for the diffraction efficiency from a volume grating (as opposed to a surface grating as in a monochromator) all assume that the variation of the change in the index of refraction is independent of the depth into the sample. This is the only situation which is analytically soluble.[26] However, Lamb waves are not uniform in the y dimension [see Eqs. (6) and (7)] and so the change in index produced by a Lamb wave is not uniform in this direction. This presents difficulties when one calculates the actual diffraction as a function of time for a given superposition. We employed a numerical integration technique to generate the simulation described below. The details of diffraction when there is spatial variation of the index in the y direction will be described in a future publication.[27] Essentially, the amplitudes of the waves that are seen in diffraction are not the amplitudes of the generated waves. Qualitatively, it is observed that modes with almost zero strain at the surface diffract more efficiently than those with finite strain at the surface. As an additional consequence of this, one does not expect a transmitted diffracted beam to display the same time dependence as a reflected diffracted beam. The observed frequencies will match, but the amplitudes will vary, giving rise to signals with different time dependencies. In a sample where the ab-

sorption is given by a Beer's law distribution, and the probe beam is incident at the Bragg angle, one will not observe antisymmetric Lamb waves due symmetry arguments. However, in the experiments reported here, the probe beam was not incident at the Bragg angle. This breaks the absorption symmetry of the probing mechanism and allows antisymmetric modes to be detected.

To illustrate the theoretical ideas discussed in this section, we compare in Fig. 4 the calculated diffracted intensity from a bulk anthracene crystal with that from an ultrathin sample. We assume heating to be the mechanism of acoustic wave generation, with an absorption coefficient $\alpha = 5\times10^3$ cm^{-1}. Figure 4(a) shows the calculated diffraction from a bulk crystal with a fringe spacing $d = 1.60\,\mu m$: one wave is excited with a frequency determined by the fringe spacing and the bulk longitudinal velocity of sound. The time dependence of the diffracted signal $\propto [1-\cos(\omega t)]$. In this example we set $V_l = 3.05\times10^5$ cm/s.[17] Figure 4(b) displays the calculated diffraction from a 2.0-μm anthracene waveguide with the same values for α and d. The beating pattern observed is primarily due to the interference between the fourth and fifth symmetric Lamb waves, with small contributions from the first three symmetric modes. Figure 4(c) demonstrates how a variation in the fringe spacing affects the observable. In Fig. 4(c), the fringe spacing was changed to 1.38 μm, all else remaining the same. The beating pattern changes because the frequencies of the excited Lamb waves change. Again, the beating is mainly the result of the interference between the fourth and fifth symmetric Lamb waves.

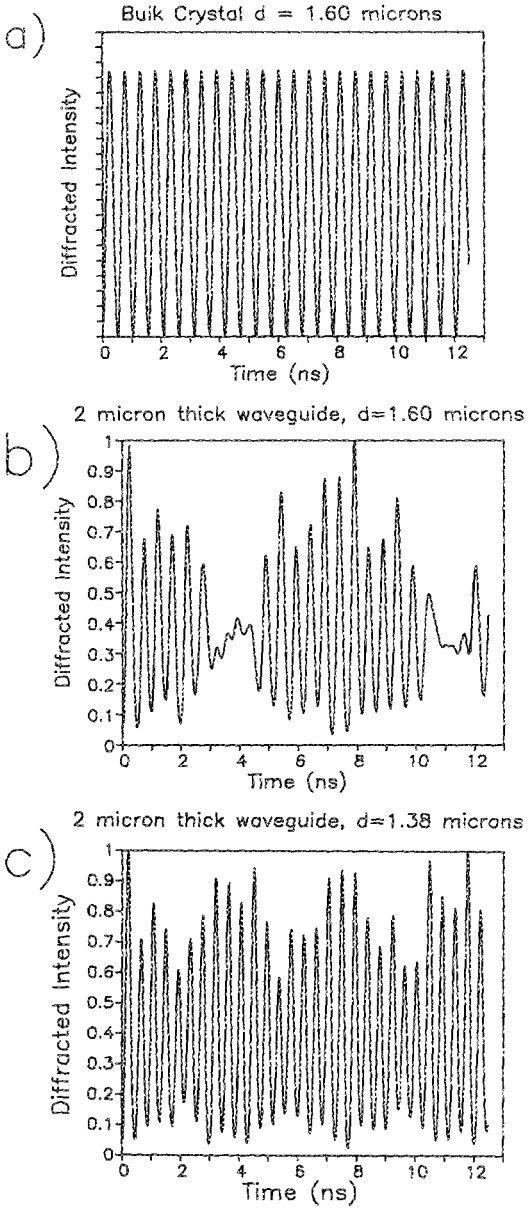

FIG. 4. (a) Calculated diffraction from a bulk anthracene crystal with $\alpha = 5\times10^3$ cm^{-1} and $d = 1.60\,\mu m$. Only one wave is excited and the time dependence of the diffracted signal $\propto [1-\cos(\omega t)]$. (b) Calculated diffraction from a 2.0-μm waveguide with $\alpha = 5\times10^3$ cm^{-1} and $d = 1.60\,\mu m$. The beating pattern results from TG excitation of several Lamb waves. (c) Calculated diffraction from the same waveguide but with $d = 1.38\,\mu m$. The change in the beating pattern is a result of changing the initial superposition of Lamb waves.

IV. EXPERIMENTAL RESULTS AND DISCUSSION

To demonstrate some of the ideas we have developed, we will interpret the response of anthracene sublimation flakes to different TG situations. Throughout the discussion, we will refer to a particular Lamb wave by its symmetry and number; i.e, S_4 will refer to the fourth symmetric Lamb wave, A_2 will refer to the second antisymmetric Lamb wave.

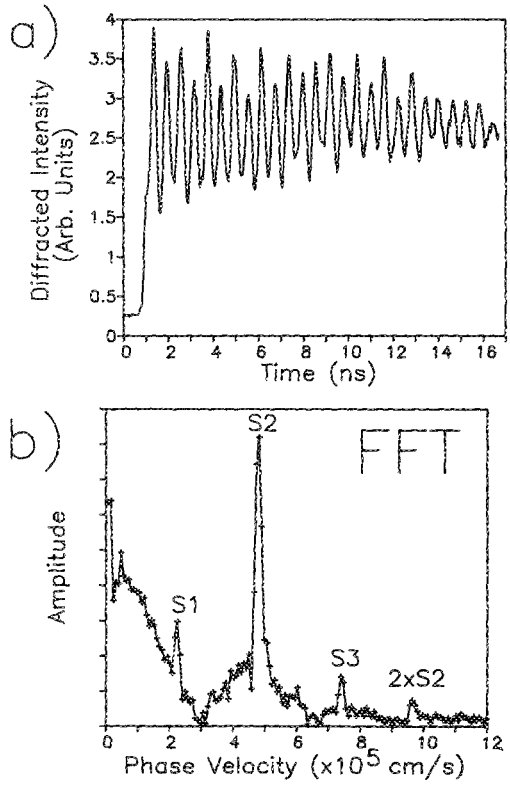

FIG. 5. Transient grating response of a 0.6-μm thick anthracene sublimation flake. Excitation and probe beams have a wavelength $\lambda = 378$ nm, and are a polarized. The grating is directed along the b axis of the crystal and $d = 2.9\,\mu m$. (a)Time domain response illustrating the characteristic beating pattern. (b)FFT clearly shows three peaks: S_1 at $\omega/\beta = 2.25\times10^5$, S_2 at $\omega/\beta = 4.83\times10^5$, and S_3 at $\omega/\beta = 7.40\times10^5$ cm/s. The second harmonic of S_2 is observed and is an artifact of the FFT procedure. The structure near $\omega = 0$ is caused by the constant offset in the time domain.

The TG response of a free-mounted anthracene sublimation flake is displayed in Fig. 5. The exciting and probing frequencies of the grating are degenerate and polarized along the a axis. Their wavelength $\lambda = 378$ nm, where the OD = 0.45 for this crystal, which is 0.6 μm thick. The grating points along the b-axis with d = 2.9 μm. In this case $\beta \times b = 1.3$. The fast Fourier transform (FFT) of this data set reveals three frequencies, with phase velocities $\omega/\beta = 2.25\times10^5$, 4.83×10^5, and 7.40×10^5 cm/s, respectively. The structure near $\omega/\beta = 0$ is due to the offset and is an artifact of the FFT. Note that none of the frequencies correspond to the bulk frequency along the b-axis: 3×10^5 cm/s given in older studies[19] or 2.80×10^5 cm/s as reported recently by Dye and Eckhardt[23]. The isotropic model predicts that the first three symmetric Lamb waves, S_1, S_2, and S_3, will be observed and that they have frequencies of $\omega/\beta = 2.16\times10^5$, 5.80×10^5, and 8.06×10^5, respectively. This is in reasonable agreement with the data considering that the anisotropic nature of the anthracene crystal is not included in the model.

Data from a mounted anthracene flake excited with a heavily damped electric field are displayed in Fig. 6. The data were taken with the wavelength of the two exciting beams at 398 nm, b polarized, and the probe wavelength at 624 nm, b polarized. The OD > 4 for this sample under these excitation conditions. The grating is aligned along the b-axis with $d = 2.28$ μm so that $\beta \times b = 5$. The crystal was 1.8 μm thick. To the eye, there is clearly a dominant frequency and a complex beating pattern displayed in the time domain data of Fig. 6(a). All of the features in the data are reproducible. In addition to the dominant frequency, the FFT of the data shown in Fig. 6(b) reveals seven other modes with significant amplitude. The dominant mode has a phase velocity of 2.82×10^5 cm/s, which is close to the bulk value reported by Dye and Eckhardt.[23] Table I compares the observed phase velocities with those predicted to have significant amplitude by the model. The agreement between observed and calculated values is quite good, especially for the A_3 mode, which is the dominant mode. As an additional example, Fig. 7 shows the FFT of the TG response of a different mounted anthracene sublimation flake. In this example $d = 2.06$ μm, the thickness of the flake is 2.0 μm, so that $\beta \times b = 6$, the excitation wavelength $\lambda = 3983$ Å and probe wavelength $\lambda = 6242$ Å. The phase velocities for the experimentally observed modes and for the theoretically predicted modes are displayed on the first line of Table II. Again, the agreement is quite good, with most modes matching to $\pm$ 0.1 cm/s. The peaks appearing in all of the figures with phase velocities less than 1×10^5 cm/s are due to difference frequencies and are an artifact of the FFT. Thus, one can conclude that mounting a flake on a fused silica substrate does not drastically alter the properties of the Lamb modes.

The reason for this lack of sensitivity to mounting is the

TABLE I. Calculated and observed phase velocities for anthracene.

	($\times10^5$ cm/s)							
Mode	A_1	S_1	A_2	S_2	A_3	S_3	S_4	A_4
Obs.	1.26	1.56	2.11	2.53	2.82	3.07	3.71	4.38
Calc.	1.07	1.36	1.90	2.34	2.78	3.23	3.70	3.99

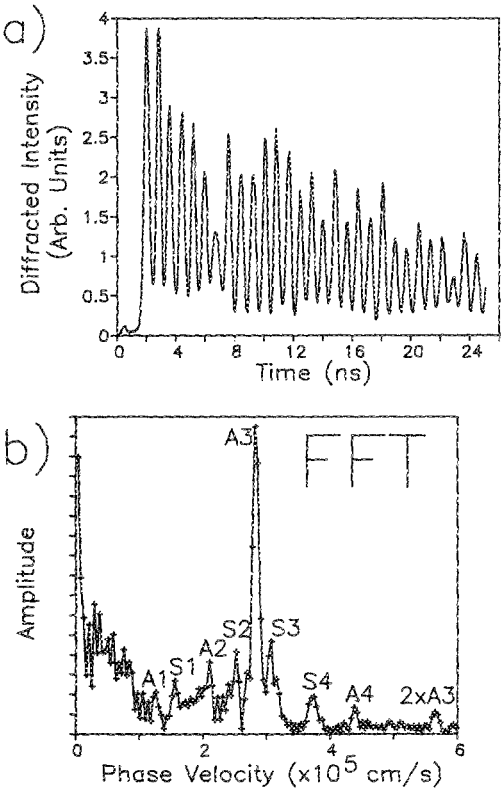

FIG. 6. Transient grating response of a mounted anthracene sublimation flake in the high OD regime. Excitation beams have a wavelength $\lambda = 398$ nm, and are b polarized; the probe beam has a wavelength $\lambda = 624$ nm, and is b polarized. The grating is directed along the crystallographic b axis and $d = 2.28$ μm. (a) Time domain response showing mainly one frequency. (b) FFT of the data shows that eight modes are excited. Mode A_3 predominates and has a phase velocity $\omega/\beta = 2.82\times10^5$ cm/s. The second harmonic is observed and labeled. Again, the structure near $\omega = 0$ is caused by the constant offset in the time domain.

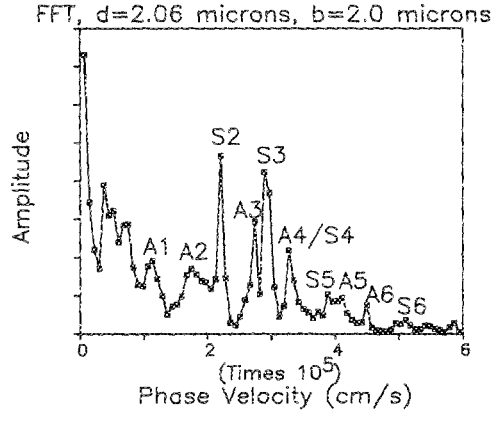

FIG. 7. The FFT of a mounted anthracene flake. The thickness of the flake was 2.0 μm. The fringe spacing was 2.06 μm and the grating was directed along the b axis. The resonant excitation pulses were polarized along the b axis with wavelength $\lambda = 3983$ Å. The probe pulse was nonresonant with wavelength $\lambda = 6242$ Å and was polarized along the b axis. The experimental and theoretical phase velocities of the labeled peaks are compared in Table II.

TABLE II. Calculated and observed phase velocities for anthracene.

Mode	A_1	S_1	A_2	S_2	A_3	S_3	A_4	S_4	A_5	S_5
	($\times 10^5$ cm/s)									
$d = 2.06\ \mu$m:										
Calc.	1.10	1.27	1.75	2.15	2.50	2.86	3.38	3.42	4.28	4.00
Obs.	1.13	1.25	1.71	2.21	2.74	2.92	3.27	···	4.12	3.90
$d = 1.60\ \mu$m:										
Calc.	1.12	1.20	1.55	1.89	2.20	2.49	2.81	3.13	3.58	3.35
Obs.	1.14	1.24	1.43	···	···	2.57	2.95	3.17	3.46	···
$d = 1.38\ \mu$m:										
Calc.	1.13	1.18	1.46	1.76	2.04	2.31	2.57	2.86	3.19	3.22
Obs.	1.00	1.23	1.51	2.00	2.11	2.41	2.76	3.00	3.25	3.32
$d = 1.21\ \mu$m:										
Calc.	1.14	1.17	1.40	1.65	1.91	2.15	2.39	2.63	2.90	3.13
Obs.	···	···	1.32	···	1.95	2.15	2.52	2.84	···	3.14
$d = 0.97\ \mu$m:										
Calc.	1.14	1.16	1.32	1.50	1.70	1.91	2.11	2.32	2.51	2.73
Obs.	···	···	1.32	1.58	···	1.95	2.12	2.28	2.61	2.89

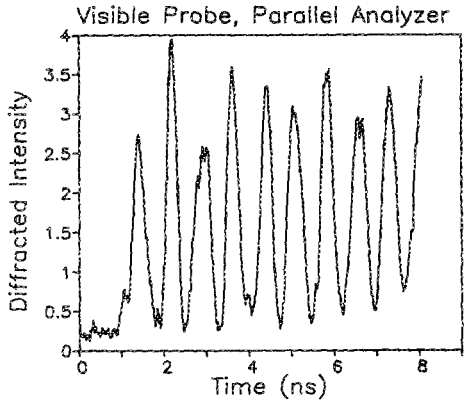

FIG. 8. Time domain response of an anthracene sublimation flake. The thickness of the flake was $\sim 0.9\ \mu$m. The fringe spacing used was $2.3\ \mu$m and the grating was directed along the b axis. The resonant excitation pulses were polarized along the a axis with wavelength $\lambda = 3977$ Å. The probe pulse was nonresonant with wavelength $\lambda = 6351$ Å and was polarized along the a axis. The analyzing polarizer was set parallel to the probe polarization.

velocity of sound in fused silica, which is 3.764×10^5 cm/s for the shear wave and 5.968×10^5 cm/s for the longitudinal wave.[16] The greater sound velocity in the substrate traps the acoustic energy in the waveguide and does not allow it to leak out. In the optical analogy, the substrate has a lower value for the index of refraction, and waves impinging on the boundary from the waveguide undergo total internal reflection. It is only when the angle of incidence is small that the wave will transmit energy into the substrate. In the acoustic case, this means that the values of k_{ts} and k_{tl} must be real and large compared to β. This occurs for modes with phase velocities greater than the bulk longitudinal phase velocity. However, the theory predicts that these modes do not contribute significantly to the initial superposition, so practically all of the acoustic energy should be trapped inside the waveguide. This allows the theory for a free, isotropic plate to be successfully applied to a mounted flake.

It is experimentally observed that when the fringe spacing is varied in the TG experiment, the phase velocities of the generated waves change. This does not happen in a bulk material, where the dispersion is a straight line. One observes a constant phase velocity independent of fringe spacing in a bulk material. In a waveguide, where the dispersion is not a straight line, the phase velocity for any one mode changes with the fringe spacing. This variation also causes the initial superposition of modes to change. As the fringe spacing is varied, it is predicted that different modes will be excited.

To demonstrate this idea, we have performed the grating experiment on a mounted anthracene sublimation flake at five different fringe spacings: 2.06, 1.60, 1.38, 1.21, and $0.97\ \mu$m. The thickness of the flake was $2.0\ \mu$m which means that $\beta \times b$ varied from 6 to 13. The FFT of the data taken with $d = 2.06\ \mu$m is displayed in Fig. 7. Modes S_2, S_3, and A_3 are observed to have the highest amplitude. The observed phase velocities for the various fringe spacings are compared to the predicted phase velocities in Table II. When $d = 1.60\ \mu$m, mode S_3 is mainly observed, with A_1 and A_4 also noticeable. As the fringe spacing is decreased to $1.38\ \mu$m, one sees that modes A_4 and S_4 are chiefly observed. At a fringe spacing of $1.21\ \mu$m, again one sees modes A_4 and S_4. When $d = 0.97\ \mu$m, one sees many modes in the FFT, including S_3, A_4, S_4, A_5, and S_5.

The observed trend is to predominantly generate the Lamb modes whose phase velocities are close to that of the longitudinal phase velocity in the bulk. This makes perfect sense, for as the thickness increases, which would make the sample more like a bulk material, $\beta \times b$ also increases. One expects that as the thickness increases, the actual bulk phase velocity would be observed. So as $\beta \times b$ increases by decreasing d, the fringe spacing, one would expect to see the same effect, namely the generation of waves with phase velocities near that of the bulk.

The effect of a resonant versus nonresonant probe and the effect of detecting the diffracted signal through an analyzing polarizer were studied on a free-mounted flake. For these data, which are displayed in Figs. 8–10, the thickness of the flake used was $\sim 0.9\ \mu$m. The fringe spacing was 2.3 μm, and the grating was directed along the crystallographic b axis (horizontal in the laboratory reference frame). The

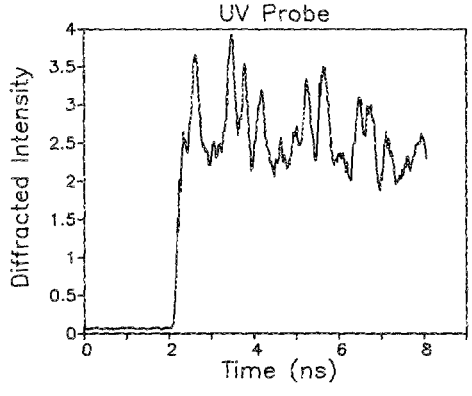

FIG. 9. Same excitation conditions as in Fig. 8, except here the probe pulse was resonant with wavelength $\lambda = 3977$ Å and was a polarized. The analyzing polarizer was again set vertically. This figure demonstrates the offset typical of all scans performed with a UV probe. The FFT of this scan shows a reduced contribution from S_2 and an increased contribution from A_1 and S_1.

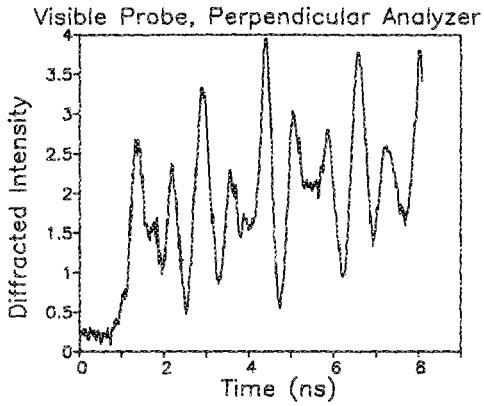

FIG. 10. Same excitation conditions as in Fig. 8, except here the probe pulse was nonresonant with wavelength $\lambda = 6351$ Å and was polarized along the a axis. The analyzing polarizer was set perpendicular to the probe polarization, thus detecting that part of the signal beam whose polarization was rotated by the grating. Additional frequency structure, due to the detection of the S_1 wave, which is shear in nature, is observed.

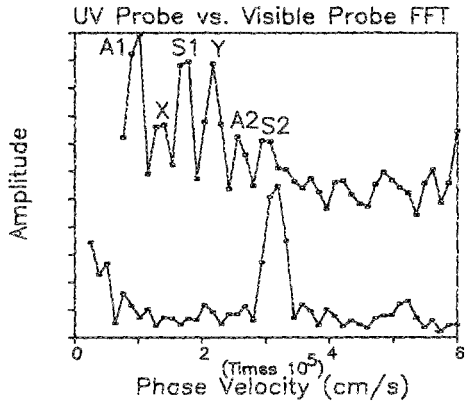

FIG. 11. The FFTs of the scans in Figs. 8 and 9 are compared. In the lower trace, the visible probe reveals mainly one frequency in the FFT, that corresponding to T_2 with $\omega/\beta = 3.1 \pm 0.1 \times 10^5$ cm/s. In the upper trace, the UV probe shows additional frequency structure. In addition to the mode detected by the visible probe, the UV probe senses two additional waves, one with $\omega/\beta = 1.0 \pm 0.1 \times 10^5$ cm/s and the other with $\omega/\beta = 1.8 \pm 0.1 \times 10^5$ cm/s. These modes correspond to the A_1 and S_1 modes, respectively, and are observed through the crossproduct between the mode's spatial dependence and the spatial dependence of the excited states and the thermal grating. The peak appearing at $\omega/\beta = 2.6 \pm 0.1 \times 10^5$ cm/s can be assigned to the A_2 mode, which has a calculated $\omega/\beta = 2.63 \times 10^5$ cm/s. Peak X can be assigned as the overtone of the A_1 mode or the difference frequency between S_2 and S_1. Peak Y can be assigned as the difference frequency between S_2 and A_1. These features and those appearing at $\omega/\beta < 0.7$ cm/s are artifacts of the FFT process.

excitation pulses were resonant with the anthracene singlet absorption and were polarized along the crystallographic a axis (vertical in the laboratory reference frame) with wavelength $\lambda = 3977$ Å. In Fig. 8, the probe pulse was nonresonant with wavelength $\lambda = 6351$ Å and was polarized along the a axis. The analyzing polarizer was set parallel to the probe polarization, i.e. vertical in the laboratory reference frame. In Fig. 9, the probe pulse was resonant with the anthracene absorption with wavelength $\lambda = 3977$ Å and was a-polarized. The analyzing polarizer was again set vertically. In Fig. 10, the probe pulse was nonresonant with wavelength $\lambda = 6351$ Å and was polarized along the a-axis. The analyzing polarizer was set perpendicular to the probe polarization, thus detecting that part of the signal beam with polarization rotated by the sample.

According to the isotropic waveguide model, three modes should be generated with significant amplitude. These modes are the first and second symmetric modes (S_1 and S_2) and the first antisymmetric mode (A_1) The first antisymmetric mode has the lowest frequency with phase velocity $\omega/\beta = 0.91 \times 10^5$ cm/s. The first symmetric mode has $\omega/\beta = 1.91 \times 10^5$ cm/s, and the second symmetric mode has $\omega/\beta = 3.24 \times 10^5$ cm/s. The A_2 mode is generated with a very small amplitude and has $\omega/\beta = 2.63 \times 10^5$ cm/s.

First, we will show that the Lamb waves which have a phase velocity ω/β which is small can be considered surface waves while those with ω/β close to the the bulk longitudinal velocity can be considered interior waves, i.e., the motion associated with the mode occurs in the middle of the waveguide. This is done by contrasting the transient grating response of the waveguide from a nonresonant probe with a resonant probe. The signal arising from a nonresonant probe will display all generated frequencies with a weighting determined by the amplitude of a particular mode and its diffraction efficiency. If the same acoustic disturbance is probed with a resonant frequency, however, the resonance will change this weighting in a predictable manner. The effect of resonance is displayed in Figs. 8, 9, and 11.

Through visual inspection of Figs. 8 and 9, it is obvious that the nonresonant probe detects a simpler acoustic disturbance than the resonant probe. In Fig. 8 one observes the acoustic waves beating against the background thermal strain. In Fig. 11 the FFTs of the scans in Figs. 8 and 9 are compared. The transient grating responses in Figs. 8–10 were only recorded for the first 8 ns, so the FFTs of these scans are not as resolved as the ones displayed in Figs. 5 and 6. From Fig. 8, the visible probe reveals mainly one frequency in the FFT, that corresponding to $\omega/\beta = 3.1 \pm 0.1 \times 10^5$ cm/s. This is assigned as the S_2 mode. Other modes are also visible with smaller amplitudes, but since they do not relate to the discussion at hand, they will not be assigned here. They are responsible for causing the amplitudes of the signal maxima in Fig. 8 to vary.

The signal obtained with the UV probe shows more frequency structure. In addition to the mode detected by the visible probe, which now has a relatively small amplitude, the UV probe senses two additional waves, one with $\omega/\beta = 1.0 \pm 0.1 \times 10^5$ cm/s and the other with $\omega/\beta = 1.8 \pm 0.1 \times 10^5$ cm/s. These modes correspond to the A_1 and S_1 modes, respectively. There is another small peak appearing with $\omega/\beta = 2.6 \pm 0.1 \times 10^5$ cm/s, which can be assigned to the A_2 mode. Peak X can be assigned as the difference frequency between S_2 and S_1. Peak Y can be assigned as the overtone of A_1 or the difference frequency between S_2 and A_1. These features and those appearing at $\omega/\beta < 0.7$ cm/s are artifacts of the FFT process.

To see that the additional modes A_1 and S_1 detected by the UV probe are indeed surface modes, it is necessary to consider Eqs. (5)–(8). When the phase velocity of a wave is lower than V_l, k_{ll} becomes imaginary. The same is true for

V_s and k_{ts}. When this occurs, the y dependence of the Lamb waves given in Eqs. (6) and (7), changes from being oscillatory (sin and cos) to being damped (sinh and cosh). Since, for A_1, $\omega/\beta = 1.0 \pm 0.1 \times 10^5$ cm/s is less than the bulk $V_s = 1.22 \times 10^5$ cm/s,[19] both k_{ts} and k_{tl} are imaginary. Similarly, for S_1, k_{ts} is real and k_{tl} is imaginary. These modes have a larger displacement at the surface of the waveguide than in the interior, while the opposite is true for S_2, which has k_{ts} real and k_{tl} near zero, and for higher modes.

When the grating is generated, using beams which are absorbed by the anthracene, excited states are produced. The spatial density of these excited states follows a Beer's law distribution from the front to the back surface of the waveguide. A nonresonant probe will not interact with the excited states and therefore the excited states will not affect the weighting of the Lamb waves observed with a nonresonant probe. However, a resonant probe will sense these excited states. The Δn_{ex} term for the diffraction efficiency [see Eq.(30)] will now be appreciable and the cross term between Δn_{ex} and Δn_p in the expression for $\Delta n(\omega)$ [see Eqs. (28) and (30)] will influence the time dependence of the signal.[10] The same argument holds for the imaginary part of the index. Since the excited states in the sample are spatially inhomogeneous, the cross term will selectively amplify the signal arising from acoustic waves whose displacements occur where the excited states exist, namely those near the front surface. This amplifies acoustic waves with imaginary values of k_{ts} or k_{tl}. Therefore modes A_1 and S_1 will be selectively amplified when the grating is probed by a resonant probe beam.

The second possible reason for the amplification of the surface modes under resonant probing conditions employs the temperature-dependent change in the index of refraction, Δn_T and Δk_T. The temperature profile of the sample will be exponential, similar to that of the excited states. If the change in the real or imaginary part of the index of refraction with temperature is large near resonance, the crossproduct between the thermal contribution and the density contribution can amplify the surface modes. This analysis would account for the fact that the offset seen in Fig. 9 does not decay with the excited state lifetime. However, since the value for the change in the index of refraction with temperature is not known for anthracene, it cannot be judged whether or not this is a valid mechanism.

Another feature of waveguide modes that can be demonstrated with this technique is the shear versus longitudinal nature of a particular mode. Starting with the velocity field expressions for the symmetric and antisymmetric Lamb waves in an isotropic medium, one can calculate the strain in the medium due to a particular wave. Only the strains S_{yy}, S_{zz}, S_{yz}, are nonzero for Lamb waves. The functional form of $\partial S/\partial t$ is as follows:

$$\frac{\partial S_{yy}}{\partial t} = \frac{1}{\beta^2}\left[-k_{tl}^2 \cos(k_{tl}y)\cos\left(\frac{k_{ts}b}{2}\right) - \left(\frac{\beta^2 - k_{ts}^2}{2}\right)\cos\left(\frac{k_{tl}b}{2}\right)\cos(k_{ts}y)\right]\cos\beta z \quad (31a)$$

$$\frac{\partial S_{zz}}{\partial t} = \frac{1}{\beta^2}\left[-\beta^2 \cos(k_{tl}y)\cos\left(\frac{k_{ts}b}{2}\right) + \left(\frac{\beta^2 - k_{ts}^2}{2}\right)\cos\left(\frac{k_{tl}b}{2}\right)\cos(k_{ts}y)\right]\cos\beta z \quad (31b)$$

$$\frac{\partial S_{yz}}{\partial t} = \frac{1}{\beta^2}\left[\beta k_{tl}\sin(k_{tl}y)\left(\frac{\cos k_{ts}b}{2}\right) + \left(\frac{(\beta^2 - k_{ts}^2)^2}{4\beta k_{ts}}\right)\cos\left(\frac{k_{tl}b}{2}\right)\sin(k_{ts}y)\right]\sin\beta z \quad (31c)$$

for the symmetric modes, and

$$\frac{\partial S_{yy}}{\partial t} = \frac{1}{\beta^2}\left[-k_{tl}^2 \sin(k_{tl}y)\sin\left(\frac{k_{ts}b}{2}\right) - \left(\frac{\beta^2 - k_{ts}^2}{2}\right)\sin\left(\frac{k_{tl}b}{2}\right)\sin(k_{ts}y)\right]\cos\beta z \quad (32a)$$

$$\frac{\partial S_{zz}}{\partial t} = \frac{1}{\beta^2}\left[-\beta^2 \sin(k_{tl}y)\sin\left(\frac{k_{ts}b}{2}\right) + \left(\frac{(\beta^2 - k_{ts}^2)}{2}\right)\sin\left(\frac{k_{tl}b}{2}\right)\sin(k_{ts}y)\right]\cos\beta z \quad (32b)$$

$$\frac{\partial S_{yz}}{\partial t} = \frac{1}{\beta^2}\left[-\beta k_{tl}\cos(k_{tl}y)\sin\left(\frac{k_{ts}b}{2}\right) - \left(\frac{(\beta^2 - k_{ts}^2)^2}{4\beta k_{ts}}\right)\sin\left(\frac{k_{tl}b}{2}\right)\cos(k_{ts}y)\right]\sin\beta z \quad (32c)$$

for the antisymmetric modes.

The dependence of the magnitude of the shear and longitudinal strains on k_{ts} and k_{tl} causes some Lamb waves to rotate the polarization of light that impinges on the grating while other Lamb waves will not do so. Notice that if k_{tl} is very small, the leading term for the shear strain S_{yz} approaches zero because the magnitude varies as the product of $\beta \times k_{tl}$. For antisymmetric modes, S_{yz} goes identically to zero for $k_{tl} = 0$. This implies that for a Lamb mode whose phase velocity is close to that of the bulk longitudinal velocity, i.e., has a small value of k_{tl}, there will be a reduced contribution to the shear strain. The second term in the expression for the shear strain increases in magnitude as k_{ts} approaches zero due to the inverse dependence of the magnitude of S_{yz} on k_{ts}. This means that a Lamb mode with a phase velocity close to the phase velocity of the bulk shear wave, which will have a small value for k_{ts}, will contribute more to the signal that is observed when the analyzing polarizer is at right angles to the polarization of the probe beam. In a bulk sample, the longitudinal wave is seen exclusively when the analyzing polarizer is aligned with the incoming polarization. The shear wave is observed only when the analyzing polarizer is perpendicular to the incoming polarization.[15] In a waveguide this separation still occurs, but not to the same extent.

This is displayed in Figs. 8, 10, and 12. Figures 8 and 10 display the transient grating response of a free-mounted anthracene sublimation flake that was probed with a nonresonant wavelength. In Fig. 8, the analyzing polarizer was aligned vertically, which passed light that was not rotated by the grating. In Fig. 10, the polarizer was rotated by 90° to

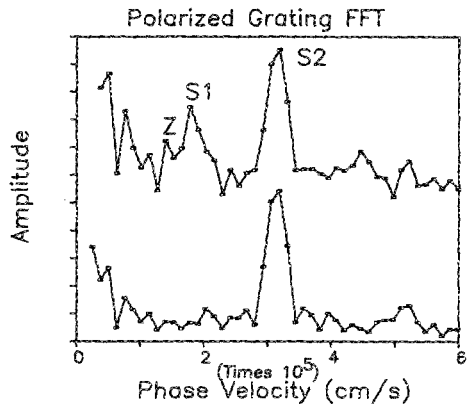

FIG. 12. The FFTs of the scans in Figs. 8 and 10 are compared. Again, in the lower trace, the visible probe reveals mainly one frequency in the FFT, that corresponding to T_2 with $\omega/\beta = 3.1 \pm 0.1 \times 10^5$ cm/s. However, by rotating the analyzing polarizer, the signal becomes more complex. There is added frequency structure which is illustrated in the top trace, which is the FFT of the scan in Fig. 10. The second mode observed in Fig. 10 is S_1 with $\omega/\beta = 1.8 \pm 0.1 \times 10^5$ cm/s. The mode with $\omega/\beta = 1.0 \pm 0.1 \times 10^5$ cm/s is not observed in this configuration because it is confined to the surface and is not detected by the nonresonant probe. Peak Z in the FFT of Fig. 10 is the difference frequency between the S_2 and S_1 modes. Again, this feature and those appearing at $\omega/\beta < 0.7$ cm/s are artifacts of the FFT process.

pass light which was rotated by the grating. It is obvious from Fig. 8 that mainly one mode is detected with the parallel configuration. This is confirmed by the bottom trace of Fig. 12, which represents the FFT of the scan in Fig. 8. However, by rotating the analyzing polarizer, the signal becomes more complex. There is added frequency structure which is illustrated in the top trace in Fig. 12, which is the FFT of the scan in Fig. 10. As mentioned above, the mode observed in Fig. 8 has a phase velocity $\omega/\beta = 3.1 \pm 0.1 \times 10^5$ cm/s and is assigned to S_2. The second mode observed in Fig. 10 has a phase velocity $\omega/\beta = 1.8 \pm 0.1 \times 10^5$ cm/s, and as above, is assigned to the S_1 mode. The mode with $\omega/\beta = 1.0 \pm 0.1 \times 10^5$ cm/s is not observed in this configuration because it is confined to the surface and is not detected by the nonresonant probe. Peak Z in the FFT of Fig. 10 is the difference frequency between the S_2 and S_1 modes. Again, this feature and those appearing at $\omega/\beta < 0.7$ cm/s are artifacts of the FFT process.

Figures 8–12 form a self-consistent picture of the Lamb modes that are generated by the excitation conditions described above. Three modes are generated. The S_2 mode has $\omega/\beta = 3.1 \pm 0.1 \times 10^5$ cm/s and is similar to the bulk longitudinal mode. It has both k_{ts} and k_{tl} real, and is seen as an interior mode. The S_1 mode has $\omega/\beta = 1.8 \pm 0.1 \times 10^5$ cm/s and has substantial shear nature. It possesses a real value for k_{ts} and an imaginary value for k_{tl}, which gives it enough surface character to be detected by the resonant probe. The A_1 mode with $\omega/\beta = 1.0 \pm 0.1 \times 10^5$ cm/s is a surface mode and both k_{ts} and k_{tl} are imaginary.

There is more theoretical evidence for associating the S_1 mode with a shear mode. In an isotropic solid, when $\omega/\beta = \sqrt{2}V_s$, the Lamb mode is a shear wave propagating at 45° with respect to the b axis. At this angle of incidence upon the surface of the flake, the shear wave is decoupled from the longitudinal mode and no mixing with the longitudinal mode takes place. This is known as the Lamé wave, and it is entirely shear in nature, with its polarization vector perpendicular to the direction of propagation and in the yz plane.[9] For this motion to occur and for the mode to be symmetric, there must be an imaginary component of k_{tl}. For the bulk shear velocity of 1.22×10^5 cm/s,[19] one calculates a Lamé velocity of 1.72×10^5 cm/s. This is close to the calculated and observed phase velocity of the S_1 mode and can be taken as further evidence of the shear nature of this mode.

It should be pointed out that the Rayleigh wave, which is a surface acoustic wave, is a superposition of the A_1 and S_1 modes. It does not truly exist until these two modes possess the same frequency. This occurs for values of $\beta \times b > 10$. The calculated Rayleigh velocity for the isotropic model of anthracene is 1.15×10^5 cm/s. The agreement between this value and the measured value of A_1 given above is strictly fortuitous. For $\beta \times b < 10$, the Rayleigh wave does not exist per se. One still has the A_1 and S_1 modes decoupled because their frequencies are not identical. In the data presented above, we observe decoupled S_1 and A_1 waves.

The agreement between calculated and observed phase velocities can be understood by considering the isotropic model in terms of the slowness curves which are characteristic of any solid. Slowness curves represent the inverse velocity of an acoustic wave propagating in a given direction in a solid.[9] They are usually presented for three planes of a solid with mutually orthogonal normals to characterize the acoustic motion in the sample. The slowness curves for an isotropic material consist of three circles: one representing the longitudinal mode and two for the shear modes. In an anisotropic solid such as anthracene, these circles deviate into ellipses and general simple closed curves.[23] In our model we assume that in anthracene these slowness curves are circles whose radii equal the inverse of the bulk sound velocity along the b axis. This assumption is reasonable as long as the direction of wave propagation is along the b axis. Any significant deviation from propagation in this direction will affect both the calculated values of the frequencies in Fig. 3 and the spatial dependence of the velocity fields in Eqs. (5)–(7).

A Lamb mode can be pictured as the coherent superposition of a shear mode and a longitudinal mode whose directions are given by the vector sum of β, which lies along the b axis, with k_{ts} and k_{tl}, respectively, which, when real, lie in the direction perpendicular to the ab plane (the y direction, see Fig. 2). So the isotropic approximation will not work well for large, real values of k_{ts} and k_{tl} because then the direction of the partial waves used in the superposition state will not lie along the b axis. However, if k_{ts} and k_{tl} are imaginary, the direction of the partial waves will still be along the b axis, and the approximation should be reasonable. Indeed, this is observed in our data. The failure of the model to predict the proper frequencies for some modes is due to the large, real values of k_{ts} for these modes. In the model, $\beta = 2.78 \times 10^4$ cm^{-1} for a fringe spacing of 2.3 μm, while k_{ts} for S_2 is 5.26×10^4 cm^{-1}, which implies a very large deviation from propagation along the b axis for that mode. This provides a very instructive demonstration of where and why

the isotropic model fails in describing the acoustic properties of an anisotropic system. The agreement between theory and experiment is reasonable because the grating is directed along the b axis.

As mentioned earlier, to reduce the effects of anisotropy, the induced grating was aligned along the b axis of the crystal. In anthracene, the b-axis is a twofold rotation axis. An individual Lamb wave can be envisioned as the coherent superposition of several bulk waves in the crystal. The image of a waveguide mode as one which bounces between two surfaces is valid in acoustics as well as optics. In the optical picture, which is typically for isotropic materials, the magnitude of the y component of the wavevector after reflecting from the front surface is identical to that after reflection from the back surface. In an arbitrarily oriented anisotropic material, however, reflection of an acoustic wave impinging on the front surface at a given angle of incidence is not the same as reflection of the same wave at the same angle of incidence at the back surface. This is because the slowness curves of the anisotropic solid will not have any symmetry with respect to the plane of the waveguide; and while the tangential component of the wavevector will always be conserved upon reflection, the magnitude and direction of the normal component of the reflected wavevector will be different for the two surfaces. By orienting the anisotropic solid, one can simplify matters. For anthracene, by placing the twofold rotation axis along the grating direction, one conserves not only the tangential component of the wavevector (β) upon reflection, but also conserves the y component (the direction perpendicular to the plane of the waveguide) of the normal component of the wavevector. So it is only the x component (aligned now with the a axis of the flake) of the normal component of the wavevector which is reflected differently at the two surfaces, and they are still related by a twofold rotation symmetry. In this instance, one would expect the normal modes to be zigzag in nature, propagating along the grating but bouncing up and down the a axis with each reflection from the surface. This is not a planar normal mode, as one obtains in an isotropic waveguide, but it is not the exceedingly complex motion that would have to be associated with an arbitrarily oriented anisotropic solid, either. Thus, by directing the grating along the b axis of the crystal, the normal modes become zigzag in nature, only slightly more complex than in an isotropic material.

If k_{ts} and k_{tl} are imaginary, there will be no zigzag motion because there is no real, normal component of the wavevector to reflect. In this instance the mode would truly be planar, and the isotropic approximation will again be reasonable.

V. CONCLUDING REMARKS

In this paper, we have discussed the mechanical response of a waveguide to optical excitation in a transient grating experiment. We have shown theoretically how the driving force in a waveguide differs from that in a bulk sample, demonstrating the influence that a finite dimension has upon the solution of the acoustic field equations. By comparing the predictions of the theory with the experimentally determined response of an anthracene sublimation flake, we have been able to elucidate the nature of the Lamb waves that were generated in the sample as well as testing the limitations of the theory. By examining the response of an optically contacted flake, we demonstrated the ability of the transient grating technique to map out dispersion relations for physical systems which are difficult to handle theoretically.

This work can be used as a guide for using this technique to perform nondestructive evaluation on delicate samples. The variation in the observable as a function of sample position at constant fringe spacing provides a means for measuring the uniformity of the thickness as a function of position. The observable also varies with residual strain in the sample, allowing one to examine the quality of optical contact. The experimental ability to measure dispersion relations will provide incentive for detailed computer modeling of anisotropic modes in waveguides. All of these factors will lead to a better understanding of waveguide phenomena and may facilitate acoustic testing of ultrathin materials and the development of waveguide devices.

ACKNOWLEDGMENTS

The authors would like to thank the National Science Foundation Division of Materials Research (DMR 87-18959) and the National Science Foundation Computing Grant (CHE 88-21737) for supporting this research.

[1] C. Kittel, *Introduction to Solid State Physics*, 5th ed. (Wiley, New York, 1976), Chaps. 4 and 5.
[2] J. R. Hardy and A. M. Karo, *The Lattice Dynamics and Statics of Alkali Halide Crystals* (Plenum, New York, 1979).
[3] R. O. Pohl, in *Amorphous Solids, Low Temperature Profiles*, edited W. A. Phillips (Springer, Berlin, 1981).
[4] G. S. Kino, Science **206**, 175 (1979); G. S. Kino, *Acoustic Waves* (Prentice Hall, Englewood Cliffs, NJ, 1987), Chap 3.
[5] C. M. Sotomayor Torres, J. C. Portal, J. C. Maan, and R. A. Stralding, *Optical Properties of Narrow-Gap Low-Dimensional Structures* (Plenum, New York, 1987).
[6] M. Munch and A. Gast, J. Chem. Soc. Faraday Trans. I (in press).
[7] G.I. Stegeman, R. Zanoni, K. Rochford, C. T. Seaton, *Nonlinear Optical Effects in Organic Polymers*, edited by J. Messier, F. Kajzar, P. Prasad, and D. Ulrich, (Plenum, New York, 1989), p. 257.
[8] M. D. Fayer, IEEE J. Quantum Elecron. **QE-22**, 1437 (1986).
[9] B. A. Auld, in *Acoustic Fields and Waves in Solids* (Wiley, New York, 1973), Vol. 2, Chap. 10; I. Viktorov, *Rayleigh and Lamb Waves, Physical Theory and Applications* (Plenum, New York, 1967).
[10] K. A. Nelson, R. Caselegno, R. J. D. Miller, and M. D. Fayer, J. Chem. Phys. **77**, 1144 (1982); K. A. Nelson, R. J. D. Miller, D. R. Lutz, and M. D. Fayer, J. Appl. Phys. **53**, 1144 (1982).
[11] K. A. Nelson and M. D. Fayer, J. Chem. Phys. **72**, 5202 (1980).
[12] C. K. Johnson and G. J. Small, in *Excited States*, edited by E. C. Lim (Academic, New York, 1982), Vol. 6, p. 97.
[13] T. Luty and C. J. Eckhardt, J. Chem. Phys. **81**, 520 (1984).
[14] T. Anderson, Ph.D. Disseration (University of Nebraska, 1985).
[15] K. A. Nelson, J. Appl. Phys. **53**, 6060 (1982).
[16] AIP Handbook, 3rd ed, edited by D. E. Gray (McGraw-Hill, New York, 1972), pp. 3–104, 1972.
[17] J. M. Turlet, P. Kottis, and M. R. Philpott, Adv. Chem. Phys. **54**, 303 (1983).
[18] H. C. Wolf, Z. Naturforsch, **13a**, 414 (1958); Obriemov, Prikotjko, Rodnikova, Zhur. Eksp. Teoret. Fiz. **18**, 409 (1948).
[19] G. K. Afanaseva, K. S. Aleksandrov, and A. I. Kitaigorodskii, Phys. Status Solidi **24**, K61 (1967); B. Dorner, E. L. Boknenkov, S. L. Chaplot, J. Kalus, I. Natkaniec, G. S. Pawley, U. Schmelzer, and E. F. Sheka, J. Phys. C **15**, 2353 (1982); H. B. Huntington, S. G. Gangoli, and J. L. Milis, J. Chem. Phys. **50**, 3844 (1969); T. Danno and H. Inokuchi, Bull. Chem. Soc. Jpn. **41**, 1783 (1968).

[20]F. B. Hildebrand, *Advanced Calculus for Applications*, 2nd ed. (Prentice Hall, Englewood Cliffs, NJ, 1976), Chap. 6.
[21]R. C. Desai, M. D. Levenson, and J. A. Barker, Phys. Rev. A **27**, 1968 (1983).
[22]R. S. Krishnan, *Thermal Expansion of Crystals* (Pergamon, New York, 1979), p. 170.
[23]R. C. Dye and C. J. Eckhardt, J. Chem. Phys. **90**, 2090 (1989).
[24]M. Born and E. Wolf, *Principles of Optics* (Pergamon, New York, 1980), Chap. 12.
[25]L. Genberg, Q. Bao, S. Gracewski, and R. J. D. Miller, Chem. Phys. **131**, 81 (1989).
[26]T. K. Gaylord, and M. G. Moharam, Appl. Phys. B **28**, 1 (1982).
[27]C. D. Marshall, J. S. Meth, and M. D. Fayer (to be published).